

Real-Time Geometry-Based Wireless Channel Emulation

Markus Hofer^{ID}, Zhinan Xu, Dimitrios Vlastaras, Bernhard Schrenk^{ID}, Member, IEEE, David L öschenbrand^{ID}, Fredrik Tufvesson^{ID}, and Thomas Zemen^{ID}, Senior Member, IEEE

Abstract—Connected autonomous vehicles and industry 4.0 production scenarios require ultrareliable low-latency communication links. The varying positions of transmitter, reflecting objects, and receiver cause a nonstationary time- and frequency-selective fading process. In this paper, we present the necessary hardware architecture and signal processing algorithms for a real-time geometry-based channel emulator, that is needed for testing of wireless control systems. We partition the nonstationary fading process into a sequence of local stationarity regions and model the channel impulse response as sum of propagation paths with time-varying attenuation, delay, and Doppler shift. We implement a subspace projection of the propagation path parameters, to compress the time-variant channel impulse response. This enables a low data-rate link from the host computer, which computes the geometry-based propagation paths, to the software defined radio unit, that implements the convolution on a field programmable gate array (FPGA). With our new architecture, the complexity of the FPGA implementation becomes *independent* of the number of propagation paths. Our channel emulator can be parametrized by all known channel models. Without loss of generality, we use a parameterization by a geometry-based stochastic channel model, due to its nonstationary nature. We provide channel impulse response measurements of the channel emulator, using the RUSK Lund channel sounder for a vehicular scenario with 617 propagation paths. A comparison of the time-variant power delay profile and Doppler spectral density of simulated and emulated channel impulse response showed a close match with an error smaller than -35 dB. The results demonstrate that our channel emulator is able to accurately emulate nonstationary fading channels with continuously changing path delays and Doppler shifts.

Manuscript received November 14, 2017; revised May 16, 2018, October 5, 2018, and November 29, 2018; accepted December 3, 2018. Date of publication December 20, 2018; date of current version February 12, 2019. This work has been conducted within the ENABLE-S3 project that has received funding from the ECSEL joint undertaking under Grant 692455. This joint undertaking receives support from the European Union's Horizon 2020 research and innovation programme and Austria, Denmark, Germany, Finland, Czech Republic, Italy, Spain, Portugal, Poland, Ireland, Belgium, France, Netherlands, U.K., Slovakia, Norway. ENABLE-S3 is funded by the Austrian Federal Ministry of Transport, Innovation and Technology (BMVIT) under the program "ICT of the Future" between May 2016 and April 2019. This work was also partially funded by the Austrian Research Funding Association (FFG) by an industrial Ph.D. and by a short term scientific mission of the COST action 15104 (IRACON). The review of this paper was coordinated by Prof. S. C. Ergen. (*Corresponding author:* Markus Hofer.)

M. Hofer, Z. Xu, B. Schrenk, D. L öschenbrand, and T. Zemen are with the Security & Communication Technologies, AIT Austrian Institute of Technology, Vienna 1210, Austria (e-mail: markus.hofer@ait.ac.at; xuzhanan@gmail.com; bernhard.schrenk@ait.ac.at; david.loeschenbrand@ait.ac.at; thomas.zemen@ait.ac.at).

D. Vlastaras and F. Tufvesson are with the Department of Electrical and Information Technology, Lund University, Lund SE-221 00, Sweden (e-mail: dimitrios@cryodev.se; fredrik.tufvesson@eit.lth.se).

Digital Object Identifier 10.1109/TVT.2018.2888914

Index Terms—Channel emulation, FPGA, geometry-based, non-stationary, non-stationary fading process, real-time, software defined radio, time-variant, time-variant frequency-selective impulse response.

I. INTRODUCTION

NETWORKED intelligent transportation systems (ITSs), connected autonomous vehicles and industry 4.0 production environments require ultra-reliable and low latency communication (URLLC) links for control algorithms communicating with sensors and actuators. 5G communication systems aim at provisioning URLLC links as one of their main targets [1], [2]. Wireless communication channels are characterized by a random non-stationary fading process, that is dependent on the position, velocity and environment of the communication device [3]–[10]. For a fully functional system, the URLLC devices must be tested jointly with the real-time control algorithm in a *repeatable* fashion and in real-time, requiring a real-time geometry-based channel emulator, which we present in this paper. Besides commercially available channel emulation solutions from Spirent [11] and Keysight/Anite [12], software defined radio (SDR) based channel emulator solutions [13]–[21] have been developed. While the channel emulator solution developed by National Instruments (NI) [13] utilizes a vector signal transceiver to emulate a multiple-input multiple-output (MIMO) channel that is based on a tap delay line (TDL) model, Vlastaras *et al.* [14] implement a TDL with two active taps and equal power for stress testing IEEE 802.11p modems. Ghiaasi *et al.* [15] use a TDL in connection with a clustering algorithm [22], [23] to reduce the number of propagation paths that have to be simultaneously emulated. In [15] the maximum number of simultaneously active delay taps is ten. Blazek *et al.* [19] extend the emulator of [15] by utilizing a sum-of-sinusoid model in connection with a discrete-time Hilbert transform to obtain bathtub, respectively half-bathtub Doppler spectra [24] for the delay taps. In [20] the work of [15] was extended using a sparse fit to extract the most important channel coefficients for a TDL model of a road intersection scenario. The emulated channel is used for modem tests. The authors of [21] present a non-stationary wireless MIMO channel model. However, the authors only consider fractional path delays and stationarity region lengths of 9 to 20 ms where the velocity is assumed to be constant. The maximum number of emulated paths is thirty-two. The channel emulator shown by MKG systems [16] allows for a maximum number of twelve delay taps.

Due to the underlying TDL model, all the emulators described above share the main drawback that path delays can only be set in integer multiples of the sampling rate. However,

real world non-stationary communication scenarios are characterized by continuously changing real valued path delays and Doppler shifts. The testing of real-time control algorithms requires updating the position and speed of the transmitter (TX) and receiver (RX) according to the laws of kinematics, and correspondingly, the wireless propagation characteristics in *real-time* with continuous variations in delay and Doppler. With this approach the real-time wireless data communication between the controller and the sensors, as well as between the controller and the actuators reflects the properties of a realistic environment and enables repeatable tests. Use cases are, e.g., (a) testing of connected autonomous vehicles, and (b) industrial production environments with mobile robots.

Kaltenberger *et al.* [25]–[27] introduce a novel channel emulation method utilizing a low-complexity, reduced-rank subspace model for geometry-based channel emulation allowing for real-valued path delays and Doppler shifts. In [28] we present a digital fixed-point field programmable gate array (FPGA) implementation of the low-complexity, reduced-rank subspace model without the radio-frequency (RF) front end. The geometry-based channel emulator can be parameterized by any channel model ranging from ray tracing (RT) [29]–[34], a geometry-based stochastic channel model (GSCM) [35]–[40], and cluster based models [22], [41], to drop-based spatial models [42]. In [43] we show first qualitative measurement results of the geometry-based channel emulator using the RUSK Lund channel sounder.

The contributions of the paper are the following:

- We introduce the concept of geometry-based channel emulation replacing the TDL as the basic building block of a channel emulator. We extend the basic geometry-based stochastic channel model (GSCM) concept by adding visibility conditions [36] and diffraction at corners of larger objects to obtain a real-time channel model, providing the path parameters for the geometry-based channel emulator.
- We partition the non-stationary fading process in a sequence of local stationarity regions with a continuous phase transition at the boundaries of the stationarity regions. Each local stationarity region is fully described by a set of propagation paths with given attenuation, delay and Doppler shift.
- We show a comprehensive analysis of the approximation error for real-time geometry-based channel emulation.
- Furthermore, we provide an exemplary single path and multi-path evaluation of the geometry-based channel emulator. The channel impulse response of our channel emulator hardware implementation is measured with the RUSK Lund channel sounder. We manually synchronize the measurements with a MATLAB simulation and provide numeric error metrics.
- We show the backward compatibility of our channel emulator by the emulation of European Telecommunications Standards Institute (ETSI) channel models. Hence, the geometry-based channel emulator can be also parameterized by stationary TDL channel models.

Organization of the Paper The system model and the emulator architecture are introduced in Section II. In Section III we investigate the approximation error of our channel emulation algorithm. The data rate reduction and the complexity reduction of our model are analyzed in Section IV. We present the measurement setup and measurement method in Section V. In

Section VI we show the validation results and in Section VII we draw conclusions.

Notation: We denote a scalar by a , a column vector by \mathbf{a} , and its i -th element with $a[i]$. Similarly, we denote a matrix by \mathbf{A} and its (i, l) -th element by $[\mathbf{A}]_{i,l}$. The superscripts $(\cdot)^*$, $(\cdot)^T$ and $(\cdot)^H$ stand for conjugate, transpose and for conjugate transpose, respectively. A diagonal matrix with elements $a[i]$ is written as $\text{diag}(\mathbf{a})$ and the absolute value of a is denoted by $|a|$. For the discrete set I , $|I|$ denotes the number of elements of I . The largest (smallest) integer that is lower (larger) than or equal to $a \in \mathbb{R}$ is denoted by $\lfloor a \rfloor$ ($\lceil a \rceil$). We denote the set of all real numbers by \mathbb{R} and the set of complex numbers by \mathbb{C} . The expectation with respect to x is denoted by $E_x\{\cdot\}$.

II. SYSTEM MODEL

We assume a single-input single-output (SISO) propagation path based channel model. The non-stationary, time-variant frequency response [44]–[47]

$$g'_{\text{Ph}}(t, f) = \sum_{p=0}^{P-1} \eta'_p(t) e^{-j2\pi\tau_p(t)f} \quad (1)$$

is described by the superposition of P individual propagation paths with time-variant path delay $\tau_p(t)$. The non band-limited physical channel is denoted by $g'_{\text{Ph}}(t, f)$. Each path is characterized by the complex time-variant weighting coefficient $\eta'_p(t) = a_p(t)e^{j2\pi\phi_p}$ with amplitude $a_p(t)$ and initial phase ϕ_p .

The non-stationary fading process can be approximated as wide-sense stationary for stationary time T_{stat} and stationarity bandwidth B_{stat} [3], [4]. We assume that the path amplitudes are constant within a stationarity region, i.e., without loss of generality, $\eta'_p(t) \approx \eta'_p$ for $0 \leq t < T_{\text{stat}}$. Furthermore, the relative velocity between transmitter and receiver is assumed constant for the interval T_{stat} . Thus, the time-variant path delay is described by a linear model

$$\tau_p(t) = \tau_p(0) - \frac{v_p}{c_0}t, \quad (2)$$

where $\tau_p(0)$ denotes the initial path delay, v_p denotes the relative velocity between transmitter and receiver per propagation path that is determined by the geometry of the scenario (see e.g. [35], [45], [48], [49] for more information) and c_0 denotes the speed of light. Defining the Doppler shift as

$$f_p = f_c \frac{v_p}{c_0}, \quad (3)$$

where f_c denotes the carrier frequency of the system, an equivalent notation of (2) can be found as

$$\tau_p(t) = \tau_p(0) - \frac{f_p}{f_c}t. \quad (4)$$

Inserting (4) in (1) we can rewrite (1) as

$$\begin{aligned} g'_{\text{Ph}}(t, f) &= \sum_{p=0}^{P-1} \eta'_p(t) e^{-j2\pi(f'+f_c)(\tau_p(0) - \frac{f_p}{f_c}t)} \\ &= \sum_{p=0}^{P-1} \eta'_p(t) e^{-j2\pi f' \tau_p(0)} e^{j2\pi f' \frac{f_p}{f_c} t} \\ &\quad \cdot e^{-j2\pi f_c \tau_p(0)} e^{j2\pi f_p t}, \end{aligned} \quad (5)$$

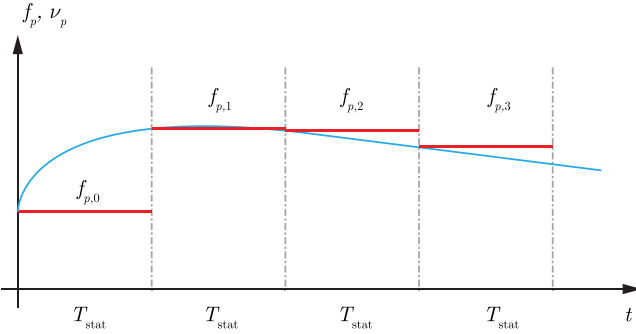


Fig. 1. Piecewise constant Doppler shift approximation of the instantaneous Doppler shift f_p for different stationarity regions.

where we consider the frequency $f = f' + f_c$ as composition of the carrier frequency f_c and the frequency offset $f' \in [-B/2, B/2]$ (see also [45, Sec. II-A]). Assuming that the system bandwidth is much smaller than the carrier frequency, i.e., $f' \ll f_c$, which is true for most communication systems [47, Ch. 1], we obtain the approximate time-variant channel transfer function (CTF) as

$$g_{\text{Ph}}(t, f) = \sum_{p=0}^{P-1} \eta_p e^{j2\pi f_p t} e^{-j2\pi \tau_p(0)f'}, \quad (6)$$

where we neglected $e^{j2\pi f' \frac{f_p}{f_c} t}$ and defined $\eta_p = \eta'_p e^{-j2\pi \tau_p(0)f'}$.

A. Non-Stationary Fading Process as Concatenation of Stationarity Regions

We emulate the channel for a finite system bandwidth B . To allow for realistic input/output filters we oversample $g_{\text{Ph}}(t, f)$ by a factor f_{OSF} , i.e., $B' = f_{\text{OSF}}B$. We sample with $T_C = 1/B'$ in time and $F_s = B'/N$ in frequency, where N is the number of frequency bins. Considering the band-limiting filters $g_{\text{TX}}(f)$ and $g_{\text{RX}}(f)$ at the transmitter and receiver side, respectively, and using (6) we obtain the sampled CTF as the concatenation of stationarity regions of length T_{stat} . Defining the length of the stationarity region in samples $M = \lceil T_{\text{stat}}/T_C \rceil$, we obtain the concatenated CTF according to

$$\begin{aligned} g[m, q] &= g_{\text{TX}}(qF_s)g_{\text{RX}}(qF_s)g_{\text{Ph}}(((s-1)M+m')T_C, qF_s) \\ &= g_{\text{TX}}[q]g_{\text{RX}}[q] \sum_{p=0}^{P-1} \eta_{p,s} e^{j2\pi \nu_{p,s} m'} e^{-j2\pi \theta_{p,s} q}, \end{aligned} \quad (7)$$

where $\eta_{p,s}, \nu_{p,s} = f_{p,s} T_C$ and $\theta_{p,s} = \tau_{p,s}(0)/(NT_C)$ denote the path weight, the normalized Doppler shift, and the normalized path delay of stationarity region s respectively. It holds that $|\nu_{p,s}| < \frac{1}{2}$ and $0 \leq \theta_{p,s} < 1$. Discrete time is denoted by $m = (s-1)M + m'$ with $m' \in \{0, \dots, M-1\}$ and discrete frequency by $q \in \{0, \dots, N-1\}$.

The velocities, and correspondingly the Doppler shifts, are assumed to be constant during a stationarity region. A schematic representation of the stationarity assumption is shown in Fig. 1. It leads to a linear change of delay within a stationarity region as modelled in (4) and shown in Fig. 2.

To allow for a continuous phase transition between stationarity regions, we incorporate the final delay of path p in region s in the starting phase of the next stationarity region $s+1$. The

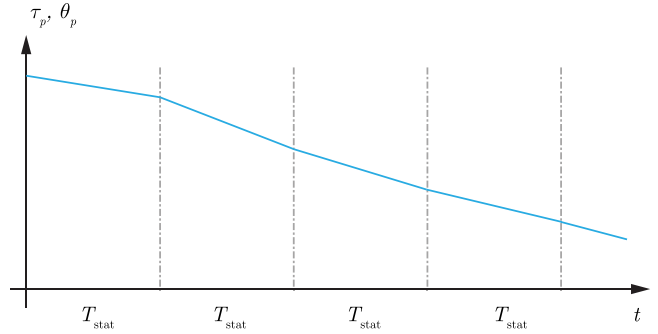


Fig. 2. Linear change of delay within stationarity regions.

delay at the end of the stationarity region is obtained by

$$\tau_{p,s}[M-1] = \tau_{p,s}[0] - \frac{f_{p,s}}{f_c} (M-1)T_C, \quad (8)$$

leading to a starting phase incorporated in $\eta_{p,s+1} = \eta_p e^{-j2\pi \tau_{p,s}[M-1] f_c}$. Correspondingly, the normalized path delay is defined as $\theta_{p,s+1} = \tau_{p,s}[M-1]/NT_C$.

To emulate the effects of a wireless propagation channel, the emulator convolves the input signal $x[m]$ with the time-variant channel impulse response (CIR) $h[m, l]$, obtaining the output signal

$$y[m] = \sum_{l=0}^{L-1} h[m-l, l]x[m-l], \quad (9)$$

with l denoting the index in the delay domain and L the number of delay taps. Due to the bandlimiting effect of the input filter, the support of $h[m, l]$ is actually infinite. However, the contributions for large l will be very small, so they can be neglected. For a causal implementation of the CIR we allow for pre- and post-cursor samples, i.e., $L = L' + L_{\text{pre}} + L_{\text{post}}$, with $L' = \lceil \tau_{\text{max}}/T_C \rceil$ and τ_{max} the maximum path delay of the CIR. The values of L_{pre} and L_{post} depend on the required dynamic range of the system.

The CIR is obtained from the inverse discrete Fourier transform (IDFT) of the time-variant CTF $g[m, q]$. For a better dynamic range of the CIR we implement a windowing function $f_{\text{win}}[q]$ (see Section V-B) that reduces the side lobes of the sinc-Kernel due to the finite bandwidth B' ,

$$h[m, l] = \frac{1}{N} \sum_{q=0}^{N-1} f_{\text{win}}[q]g[m, q]e^{j2\pi qlq/N}. \quad (10)$$

Calculating (7) is of high computational complexity, since for each time instant m' and for each frequency index q a sum of P complex exponentials (CEs) has to be calculated. In the next section we present a geometry-based channel emulator architecture that enables a real-time implementation.

B. Geometry-Based Channel Emulation Architecture

We present the structure of our geometry-based channel emulator in Fig. 3. The emulator consists of a propagation module that is implemented on a general purpose multi-core personal computer (PC) and a convolution module that is implemented on an SDR equipped with an FPGA.

The propagation module is parametrized by the channel model, which periodically updates the geometry and calculates

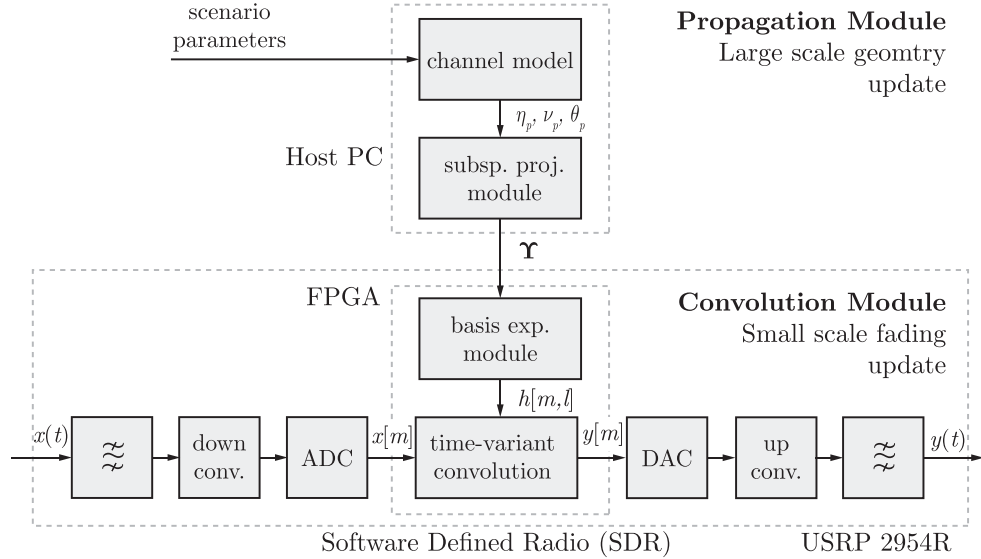


Fig. 3. Geometry-based channel emulator structure.

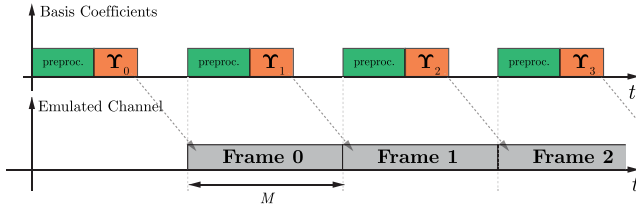


Fig. 4. Frame structure of periodic transmission of basis coefficients for stationarity regions s .

the propagation path parameters $\eta_{p,s}$, $\nu_{p,s}$ and $\theta_{p,s}$ for each stationarity region s . To reduce the computational complexity of the sum of complex exponentials (SoCE) in (7), we exploit (a) the bandlimited properties of the fading process, and (b) the limited accuracy of the analog-to-digital converter (ADC) and digital-to-analog converter (DAC) at the input and output. We approximate the SoCE in (7) by a reduced rank basis-expansion model (BEM) [25]–[28]. The BEM uses discrete prolate spheroidal (DPS) sequences [50] and the propagation parameters to calculate the basis coefficient matrix Υ_s using a subspace projection. The basis coefficient matrix describes the evolution of the channel in the time and the frequency domain in a compressed form. A schematic representation of the transmission protocol of the basis coefficients Υ_s from the PC to the SDR unit is shown in Fig. 4.

The SDR consists of a radio frequency (RF) frontend in connection with an FPGA. In the RF frontend, the input signal is filtered and converted from passband to baseband by mixing with a local oscillator (LO). It is sampled by the ADC to obtain the digital baseband signal $x[m]$. On the FPGA, we utilize Υ_s in the basis-expansion module to obtain the time-variant CIR $h[m,l]$. In the time-variant convolution module, the input signal $x[m]$ is convolved with $h[m,l]$, to obtain the output signal $y[m]$. Subsequently, $y[m]$ is converted to an analog-signal, by the DAC and shifted to the passband by mixing with the LO. Our emulator structure has two major advantages:

- The reconstruction complexity to obtain the time-variant CIR is *independent* of the number of propagation paths, which makes the model very suitable for an implementation on an FPGA.

- The streaming bandwidth between the general purpose PC and the SDR can be *significantly reduced*, since we transmit a compressed CIR in form of the basis coefficients Υ_s instead of the full CIR.

We will explain the approximation steps of the model in the next subsections in more detail. The approximation error is analyzed in Section III. For the discussion below we consider a single stationarity region s , without loss of generality.

C. Basis Expansion Model

Our reduced-rank BEM is based on two assumptions. Firstly, we assume that the channel is reconstructed block-wise for limited time-frequency snapshots, defined by the Cartesian index set

$$\mathcal{I} = I^t \times I^f = [0, \dots, M-1] \times [0, \dots, N-1]. \quad (11)$$

The size of the index set is smaller than, or equal to, the size of the local stationarity region. Secondly, we assume that ν_p and θ_p are limited to a band-limiting region that is defined by the Cartesian product

$$\mathcal{W} = W^t \times W^f = [-\nu_{D\max}, \nu_{D\max}] \times [0, \theta_{P\max}]. \quad (12)$$

Here, $\nu_{D\max} = T_C f_c v_{\max}/c_0$ where v_{\max} denotes the maximum relative velocity between transmitter and receiver, and $\theta_{P\max} = \tau_{\max}/(N T_C)$ where τ_{\max} is the maximum path delay of the channel. The maximum velocity and delay are determined by the considered scenario.

The index-limiting region \mathcal{I} in (11) and the band-limiting region \mathcal{W} in (12) are represented as Cartesian products. Hence, the subspace of the time-variant CTF for the duration of a stationarity region can be represented by two-dimensional DPS sequences [25], [28], [44], [50], [51]. DPS sequences are band-limited to a support W and simultaneously most energy concentrated in an interval I , which makes them ideally suited for reconstructing the channel within a band- and index-limited region.

The two-dimensional reconstruction shown by Kaltenberger *et al.* [25], [51] has the disadvantage, that either the two-dimensional DPS sequences have to be stored on the FPGA, which requires a lot of memory, or the two-dimensional

DPS sequences have to be calculated at run-time which is computationally expensive. Hence, for an implementation on the FPGA, we approximate (7) by a separate one-dimensional reconstruction approach shown in (13) (see above),

$$\begin{aligned} g[m', q] &\approx \hat{g}[m', q] \\ &= \sum_{p=0}^{P-1} \eta_p \sum_{k=0}^{D^f-1} u_k[q; W^f, I^f] \epsilon_{k,p} \sum_{i=0}^{D^t-1} u_i[m'; W^t, I^t] \gamma_{i,p} \\ &= \sum_{k=0}^{D^f-1} u_k[q; W^f, I^f] \sum_{i=0}^{D^t-1} u_i[m'; W^t, I^t] \underbrace{\sum_{p=0}^{P-1} \eta_p \gamma_{i,p} \epsilon_{k,p}}_{\psi_{i,k}} \\ &= \sum_{i=0}^{D^t-1} \sum_{k=0}^{D^f-1} u_i[m'; W^t, I^t] u_k[q; W^f, I^f] \psi_{i,k} \end{aligned} \quad (13)$$

with the two-dimensional basis coefficients

$$\psi_{i,k} = \sum_{p=0}^{P-1} \eta_p \gamma_{i,p} \epsilon_{k,p}. \quad (14)$$

The DPS sequences $u_j[l; W, I]$ are the solution to the eigenvalue problem [50], [52]

$$\sum_{l=0}^{M-1} C[l-m; W, I] u_j[l; W, I] = \lambda_j(W, I) u_j[m; W, I] \quad (15)$$

with $m \in I$,

$$C[k; W, I] = \int_W e^{j2\pi k\nu} d\nu = \frac{1}{j2\pi k} (e^{j2\pi k\nu_2} - e^{j2\pi k\nu_1}), \quad (16)$$

and $W = [\nu_1, \nu_2]$.

The variables $\gamma_{i,p}$ and $\epsilon_{k,p}$ denote the basis coefficients of path p in the time domain and the frequency domain, respectively. The dimensions D^t and D^f represent the number of utilized DPS sequences in the time and the frequency domain, respectively and determine the accuracy of the model. The time-variant transfer function can be efficiently compressed by a few subspace dimensions [50], [53]. That is because the eigenvalues $\lambda_j(W, I)$ of the vectorized DPS sequences $u_j(W, I)$ are clustered near 1 for $D' \leq \lceil (\nu_2 - \nu_1)|I| \rceil$ and decay exponentially to 0 for $D' > \lceil (\nu_2 - \nu_1)|I| \rceil$. Specifically, the eigenvalues $\lambda_i(W^t, I^t)$ of the vectorized DPS sequences $u_i(W^t, I^t)$ are clustered near 1 for $D'^t \leq \lceil 2\nu_{Dmax} M \rceil$ and decay exponentially to 0 for $D'^t > \lceil 2\nu_{Dmax} M \rceil$. The same holds true for the eigenvalues $\lambda_i(W^f, I^f)$.

The computational complexity for the evaluation of the reduced-rank BEM in (13) is *independent* of the number of propagation paths. This makes it suitable for an implementation on the FPGA. The separate one-dimensional structure in the time and the frequency domain allows an efficient implementation on the FPGA with a reconstruction accuracy that is equivalent to the two-dimensional approach.

D. Approximate Basis Projection

The basis coefficients $\gamma_{i,p}$ and $\epsilon_{i,p}$ have to be calculated for each path by the projection of the CEs onto the DPS sequences. The projection of a single CE $e_p(\nu_p) = [e^{2\pi j \nu_p 0}, \dots, e^{2\pi j \nu_p (M-1)}]^T$ with normalized Doppler ν_p onto the basis

functions $u_d(W, I) = [u_d[0; W, I], u_d[1; W, I], \dots, u_d[M-1; W, I]]^T$ with band-limiting regions W and index set I ,

$$\gamma_d(\nu_p; W, I) = \sum_{m'=0}^{M-1} u_d[m'; W, I] e^{j2\pi \nu_p m'} \quad (17)$$

does not lead to a reduction in computational complexity, because each CE has to be evaluated for the projection and the numerical calculation complexity persists.

In [25], [26] it is shown that for the projection of a CE onto DPS sequences discrete prolate spheroidal wave functions (DPSWFs) can be utilized. There exists a close relation between DPSWFs and DPS sequences. The amplitude spectrum of a DPS sequence $u_d[m'; W, I]$ index limited to a set $I = [0, \dots, M-1]$ and band-limited to $W = [W_0 - W_{max}, W_0 + W_{max}]$, with W_{max} being the symmetric support and $W_0 = \frac{\nu_2 - \nu_1}{2}$ the center point, is a scaled version of the associated wave function (cf. [50, equation (26)], [25], [26])

$$U_d(\nu; W, I) = \beta_d \sum_{m'=0}^{M-1} u_d[m'; W, I] e^{-j\pi(M-1-2m')\nu}, \quad (18)$$

where $\beta_d = 1$ if d is even and $\beta_d = j$ if d is odd. Comparing (17) with (18), one can see that the basis coefficients in (17) can be calculated by [25], [26]

$$\gamma_d(\nu_p; W, I) = \frac{1}{\beta_d} e^{j\pi(M-1)\nu_p} U_d(\nu_p; W, I). \quad (19)$$

For $\nu_p \in W$ approximate DPSWFs can be defined according to [25], [26]

$$\tilde{U}_d(\nu_p; W, I) = \pm e^{2\pi j(M-1+m_p)W_0} \sqrt{\frac{\lambda_d M}{2W_{max}}} u_d[m_p](W, I), \quad (20)$$

with $\lambda_d(W, I)$ the corresponding eigenvalues and

$$m_p = \left\lfloor 1 + \left(\frac{\nu_p - W_0}{W_{max}} \right) \frac{M}{2} \right\rfloor. \quad (21)$$

The sign in (20) is taken such that the normalization

$$\tilde{U}_d(W_0; W, I) \geq 0, \quad \left. \frac{d\tilde{U}_d(\nu_p; W, I)}{d\nu_p} \right|_{\nu_p=W_0} \geq 0 \quad d = 0, \dots, D-1 \quad (22)$$

holds. With (20)–(22) it can be shown that (19) can be approximately calculated by [25], [26]

$$\tilde{\gamma}_d(\nu_p; W, I) = \frac{1}{\beta_d} e^{j\pi(M-1)\nu_p} \tilde{U}_d(\nu_p; W, I). \quad (23)$$

We implement (23) using a table lookup with a table consisting of DPS sequences that can be pre-calculated and stored. We obtain the table index by inserting ν_p and θ_p into (21) and using the support W^t and W^f respectively.

Hence, the basis coefficients $\gamma_{i,p}$ and $\epsilon_{i,p}$ of each path can be approximately calculated by scaled and shifted approximate DPS wave functions with a complexity of $\mathcal{O}(1)$. Equation (23) allows for a strong computational complexity reduction compared to (17). This enables a real-time calculation of the approximate two dimensional basis coefficients $\tilde{\psi}_{i,k}$ similar to (14).

The two-dimensional basis coefficients $\tilde{\psi}_{i,k}$ represent an efficiently compressed version of the time-variant CTF in the time and the frequency domain for one stationarity region. They are

utilized to reconstruct the CIR on the FPGA as shown in the next Section.

E. Time-Variant Channel Impulse Response

First we define the vector

$$\tilde{\mathbf{g}}[m'] = [\tilde{g}[m', 0], \dots, \tilde{g}[m', N-1]]^T \in \mathbb{C}^{N \times 1}, \quad (24)$$

collecting all samples of the frequency response at time index m' , where $\tilde{g}[m', q]$ is obtained from (13) using $\tilde{\psi}_{i,k}$ instead of $\psi_{i,k}$. The time-variant CIR vector

$$\tilde{\mathbf{h}}[m'] = [\tilde{h}[m', 0], \dots, \tilde{h}[m', L-1]]^T \in \mathbb{C}^{L \times 1} \quad (25)$$

is obtained by

$$\tilde{\mathbf{h}}[m'] = \mathbf{D}^H \mathbf{P} \mathbf{F} \tilde{\mathbf{g}}[m'], \quad (26)$$

where

$$\mathbf{F} = \text{diag}(\mathbf{f}_{\text{win}}) \in \mathbb{C}^{N \times N} \quad (27)$$

with $\mathbf{f}_{\text{win}} = [f_{\text{win}}[0], f_{\text{win}}[1], \dots, f_{\text{win}}[N-1]]^T \in \mathbb{C}^{N \times 1}$ being the windowing function. The permutation matrix $\mathbf{P} \in \mathbb{R}^{N \times N}$ rearranges the elements of a vector $\mathbf{x} = [x[0], x[1], \dots, x[N-1]]^T \in \mathbb{C}^{N \times 1}$ according to

$$\mathbf{x}' = \mathbf{P}\mathbf{x} = [x[N/2], \dots, x[N-1], x[0], \dots, x[N/2-1]]^T \quad (28)$$

to fit with the subsequent IDFT. Matrix $\mathbf{D} \in \mathbb{C}^{N \times L}$ is a $N \times L$ submatrix of the Fourier matrix $[\mathbf{W}]_{i,j} = \frac{1}{\sqrt{N}} e^{-j2\pi i j} \in \mathbb{C}^{N \times N}$ and $\forall i, j \in \{0, \dots, N-1\}$.

Defining

$$\mathbf{f}^t[m'] = [u_0[m'; W^t, I^t], \dots, u_{D^t-1}[m'; W^t, I^t]]^T \in \mathbb{R}^{D^t \times 1} \quad (29)$$

and the matrix of generalized basis coefficients

$$\tilde{\Psi} = \begin{pmatrix} \tilde{\psi}_{0,0} & \dots & \tilde{\psi}_{0,D^f-1} \\ \vdots & \ddots & \vdots \\ \tilde{\psi}_{D^t-1,0} & \dots & \tilde{\psi}_{D^t-1,D^f-1} \end{pmatrix} \in \mathbb{C}^{D^t \times D^f} \quad (30)$$

we can rewrite the subspace model in (13) in matrix-vector notation as

$$\tilde{\mathbf{g}}[m'] = \mathbf{V} \tilde{\Psi}^T \mathbf{f}^t[m'], \quad (31)$$

where $\mathbf{V} = [\mathbf{u}_0(W^f, I^f), \mathbf{u}_1(W^f, I^f), \dots, \mathbf{u}_{D^f-1}(W^f, I^f)] \in \mathbb{C}^{N \times D^f}$ is the basis vector matrix in the frequency domain and $\mathbf{u}_k(W^f, I^f) = [u_k[0; W^f, I^f], \dots, u_k[N-1; W^f, I^f]]^T$. Inserting (31) in (26) we obtain

$$\tilde{\mathbf{h}}[m'] = \underbrace{\mathbf{D}^H \mathbf{P} \mathbf{F} \mathbf{V}}_{\mathbf{V}'} \tilde{\Psi}^T \mathbf{f}^t[m']. \quad (32)$$

Since the matrices \mathbf{D} , \mathbf{P} , \mathbf{F} and \mathbf{V} are constant they can be pre-calculated as $\mathbf{V}' = \mathbf{D}^H \mathbf{P} \mathbf{F} \mathbf{V}$ with $\mathbf{V}' \in \mathbb{C}^{L \times D^f}$ and stored.

The basis expansion coefficients $\tilde{\Psi}$ do not change within one stationarity region. Thus we can pre-calculate the multiplication with the matrix \mathbf{V}'

$$\Upsilon = \mathbf{V}' \tilde{\Psi}^T, \quad \Upsilon \in \mathbb{C}^{L \times D^t} \quad (33)$$

and reformulate (32) as

$$\tilde{\mathbf{h}}[m'] = \Upsilon \mathbf{f}^t[m']. \quad (34)$$

The basis vectors $\mathbf{f}^t[m']$ are stored on the FPGA memory and are used for the reconstruction of the CIR.

III. ERROR ANALYSIS

In this section we analyze the error of the geometry-based channel emulator that is based on the reduced-rank BEM. Without loss of generality, we model the error within one stationarity region s . The error has to be smaller than the numerical precision, determined by the fixed-point precision of the analog/digital converter. It is defined by

$$E_{\text{th}} = 2^{-(N_b - 1)}, \quad (35)$$

where N_b is the number of bits of the analog-to-digital converter. We analyze the following error sources:

- The basis expansion model bias,
- the approximate basis projection error,
- the error due to the piecewise constant Doppler assumption, and
- the narrowband approximation error.

A. Basis Expansion Model Bias

The reduced-rank BEM in (13) leads to an approximation bias that depends on the number of DPS sequences D^t and D^f that are utilized in the time and the frequency direction, respectively. For an uniform distribution of ν_p and θ_p on W^t and W^f , respectively, it can be shown [25], [28], [51] that

$$\text{bias}^2(D^t) = \frac{1}{2\nu_{\text{Dmax}} M} \sum_{i=D^t}^{M-1} \lambda_i(W^t, I^t), \quad \text{and} \quad (36)$$

$$\text{bias}^2(D^f) = \frac{1}{\theta_{\text{Pmax}} N} \sum_{k=D^f}^{N-1} \lambda_k(W^f, I^f), \quad (37)$$

where $\lambda_i(W^t, I^t)$ and $\lambda_k(W^f, I^f)$ are the sorted eigenvalues of the one dimensional DPS sequences in time- and frequency-direction respectively. In [25], [26], [28] the calculation of the optimum number of dimensions for the two-dimensional fading process described by (11) and (12) is shown.

B. Approximate Basis Projection Bias

The accuracy of the approximate projection (23) increases with reduced bandwidth W_{max} and increased number of samples M [25]. This fact is utilized by defining a resolution factor r and using DPS sequences that are oversampled for the calculation in (23). Specifically, for positive integers r we define DPS sequences with

$$I_r = [0, \dots, rM-1], \quad (38)$$

and

$$W_r = \left[W_0 - \frac{W_{\text{max}}}{r}, W_0 + \frac{W_{\text{max}}}{r} \right]. \quad (39)$$

We use $U_d(\frac{\nu_p}{r}; W_r, I_r)$ and $u_d(\frac{\nu_p}{r}, W_r, I_r)$ for calculating the approximated coefficients.

The square bias of the approximate subspace projection is defined as [25]

$$\text{bias}_{\tilde{\mathbf{g}}^{D,r}}^2 = \mathbb{E} \left\{ \frac{1}{MN} \|\mathbf{g} - \tilde{\mathbf{g}}^{D,r}\|^2 \right\}, \quad (40)$$

TABLE I
CHANNEL PARAMETERS

Parameter	Value
f_c	5.7 GHz
τ_{max}	1.6 μ s
v_{max}	400 km/h
B	10 MHz
f_{OSF}	2
T_C	50 ns
f_{pmax}	2.11 kHz
T_{stat}	256 μ s
a	-20 ... 20 m/s ²
N	128
M	5120

TABLE II
EMULATION PARAMETERS

Parameter	Value
L_{pre}, L_{post}	4
E_{th}^2	-60 dB
D^t	6
D^f	47
r_t	4
r_f	4096

with $\tilde{\mathbf{g}}^{D,r}$ (cf. [25], [28]) being the approximate DPS subspace representation. No analytical results are available for the square bias, however, for the minimum square bias achievable it was numerically conjectured in [25] that

$$\text{bias}_{\min,r}^2 = \min_D \text{bias}_{\tilde{\mathbf{g}}^{D,r}}^2 \approx \left(\frac{2W_{\max}}{r} \right)^2, \quad (41)$$

with $2W_{\max}$ representing the maximum two sided support. We use this as a guideline to calculate the resolution factors in time direction r^t and in frequency direction r^f separately. The resolution factors have to be chosen such that the bias is smaller than E_{th}^2 . We refer the reader to [25], [27], [28] for additional information on the resolution factor. For the parameters in Table I and E_{th}^2 from Table II we obtain $r^t = 4$ and $r^f = 4096$.

C. Error Analysis of the Piecewise Constant Doppler Assumption

We investigate the error of the CTF due to the piecewise constant velocity (and Doppler shift) assumption within one stationarity region. For the analysis we consider the comparison with a scenario with constant acceleration a , which causes a linear changing velocity (Doppler shift). We model the error of a single propagation path with zero path delay. The linear changing velocity is modelled by

$$v_p[m'; a] = v_0 + am'T_C, \quad (42)$$

with the relative velocity v_0 between TX and RX. Thus,

$$\begin{aligned} \nu_p[m'; \Delta f_p(a, f_c)] &= \frac{v_p[m'; a]}{c_0} f_c T_C \\ &= \frac{(v_0 + am'T_C)}{c_0} f_c T_C \\ &= \underbrace{\frac{v_0}{c_0} f_c T_C}_{\nu_p} + \underbrace{\frac{a}{c_0} f_c T_C^2 m'}_{\Delta f_p(a, f_c)}, \end{aligned} \quad (43)$$

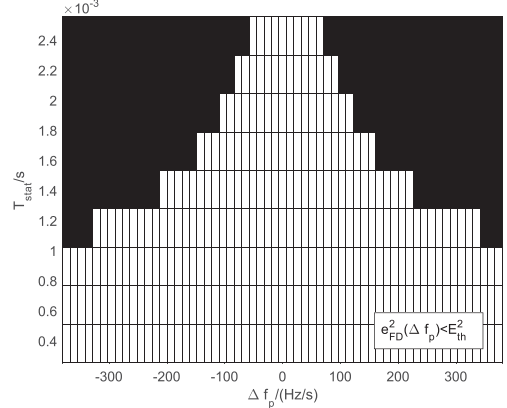


Fig. 5. Error $e_{FD}^2(\Delta f_p)$ for piecewise constant Doppler shift vs. Doppler shift change and stationarity region length T_{stat} . The white region shows the area where $e_{FD}^2(\Delta f_p) < E_{th}^2$.

where $\Delta f_p(a, f_c)$ denotes the Doppler shift change of propagation path p . With a slight misuse of notion we obtain for the CTF

$$g[m'; \Delta f_p] = e^{j2\pi(\nu_p + \Delta f_p T_C^2 m')m'}. \quad (44)$$

The mean square error (MSE) is calculated by

$$\begin{aligned} e_{FD}^2(\Delta f_p) &= \frac{1}{M} \sum_{m'=0}^{M-1} |g[m'; 0] - g[m'; \Delta f_p]|^2 \\ &= \frac{1}{M} \sum_{m'=0}^{M-1} |e^{j2\pi\nu_p m'} (1 - e^{j2\pi\Delta f_p T_C^2 m'^2})|^2 \\ &= \frac{1}{M} \sum_{m'=0}^{M-1} |(1 - e^{j2\pi\Delta f_p T_C^2 m'^2})|^2. \end{aligned} \quad (45)$$

The implementation of the approximated channel emulation requires $e_{FD}^2(\Delta f_p) < E_{th}^2$. An example evaluation of the error with the parameters of Table I is shown in Fig. 5.

We consider a maximum acceleration of ± 20 m/s², which leads to $\Delta f_p \in \{-380.3 \text{ Hz/s}, \dots, 380.3 \text{ Hz/s}\}$. For the stationarity region lengths we evaluate $T_{stat} \in \{256 \mu\text{s}, 512 \mu\text{s}, \dots, 2.56 \text{ ms}\}$. We consider $E_{th}^2 = -60$ dB for the error threshold (cf. Table II).

The white region in Fig. 5 represents the area where $e_{FD}^2(\Delta f_p) < E_{th}^2$. We observe that there is a trade-off between Δf_p and T_{stat} . Considering a fixed error threshold a large Δf_p requires small T_{stat} , and vice versa. Please note that Δf_p depends on f_c and a (cf. (43)). Hence, considering Δf_p fixed, to meet a fixed error threshold, an increase of the center frequency requires the reduction of the maximum acceleration and vice versa.¹ We choose $T_{stat} = 256 \mu\text{s}$ so that $e_{FD}^2(\Delta\nu_P(a)) < E_{th}^2$ for the example implementation with E_{th}^2 defined in Table II in this paper.

The parameters of Table I are utilized for numerical evaluation to set up the DPS sequences as described in Section II-C (cf. (11) and (12)).²

¹The maximum length of the stationarity region is ultimately limited by the complexity and storage of the used FPGA and the required accuracy of the channel model.

²We select the velocity $v_{max} = 400$ km/h (111 m/s) in Table I such that a large variety of scenarios can be emulated, i.e., also highway scenarios with high relative velocities. All scenarios with a velocity smaller than v_{max} can be emulated by this setup.

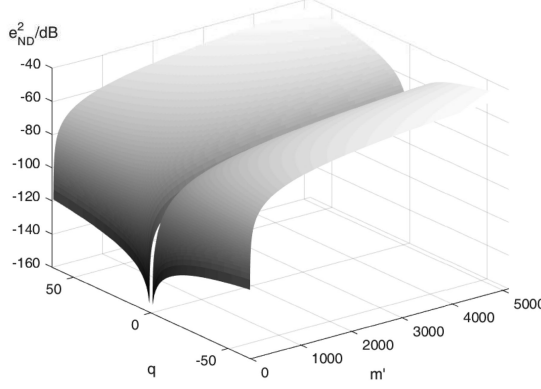


Fig. 6. Exemplary narrowband approximation error vs. time and frequency index for $f_{\text{pmax}} = 2.11 \text{ kHz}$, $T_{\text{stat}} = 256 \mu\text{s}$, $f_c = 5.7 \text{ GHz}$, and $T_C = 50 \text{ ns}$ (cf. Table I).

D. Narrow Band Approximation Error

In this Section we investigate the error caused by neglecting $e^{j2\pi \frac{f_p}{f_c} t f'}$ in the CTF in (5). We sample (5) with $T_C = 1/B'$ in time direction and $F_s = B'/N$ in frequency direction and use the definition of η_p in (6). Using the definition of $g[m, q]$ in (7), considering one stationarity region and neglecting the band-limiting filter $g_{\text{TX}}[q]$ and $g_{\text{RX}}[q]$ we obtain

$$g'[m', q] = g[m', q] e^{j2\pi \frac{f_p}{f_c} \frac{m' T_C q}{N T_C}} \quad (46)$$

$$= g[m', q] e^{j2\pi \frac{f_p}{f_c} \frac{m' q}{N}}. \quad (47)$$

We define the normalized error per time and frequency index by

$$\begin{aligned} e_{\text{NB}}^2(f_p; m', q) &= |g[m', q] - g'[m', q]|^2 / |g[m', q]|^2 \\ &= \left| g[m', q] \left(1 - e^{j2\pi \frac{f_p}{f_c} \frac{m' q}{N}} \right) \right|^2 / |g[m', q]|^2 \\ &= \left| \left(1 - e^{j2\pi \frac{f_p}{f_c} \frac{m' q}{N}} \right) \right|^2. \end{aligned} \quad (48)$$

An example representation of the error with the parameters of Table I is shown in Fig. 6. We observe that the error grows with time and frequency index and increasing Doppler shift. For Doppler shifts small compared to the carrier frequency and small stationarity regions the error can essentially be neglected. For the emulation of larger Doppler shifts, the error may lead to a small phase discontinuity at the stationarity region boundaries.

For the design of the channel emulator we choose the parameters such that $e_{\text{FD}}^2(\Delta f_p) + e_{\text{NB}}^2 + \text{bias}^2(D^t) + \text{bias}^2(D^f) < E_{\text{th}}^2$.

IV. DATA RATE AND COMPLEXITY ANALYSIS

A. Data Rate Analysis for PC-SDR Link

The compression of the CIR in terms of basis expansion coefficients leads to an effective bandwidth reduction for the communication link between PC and SDR. Streaming the full CIR $h[m, l]$ at each time instant m requires

$$R_{\text{full}} = \frac{2 L N_{\text{bit1}}}{T_C} \text{ bits/s}, \quad (49)$$

while streaming the compressed CIR using Υ_s requires

$$R_{\text{comp}} = \frac{2 L D^t N_{\text{bit2}}}{T_{\text{stat}}} \text{ bits/s}. \quad (50)$$

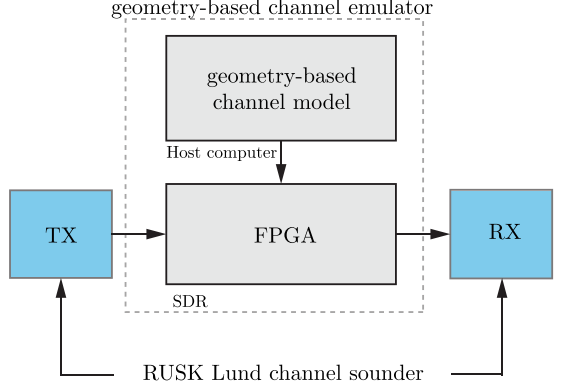


Fig. 7. Measurement setup for the validation.

N_{bit1} and N_{bit2} correspond to the used fixed-point precision for streaming $h[m, l]$ and $[\Upsilon_s]_{k,l}$ to the SDR unit, respectively. Comparing the two data rates we obtain the data rate reduction factor

$$r_{\text{red}} = \frac{R_{\text{full}}}{R_{\text{comp}}} = \frac{T_{\text{stat}} N_{\text{bit1}}}{D^t T_C N_{\text{bit2}}}. \quad (51)$$

Since $T_C \ll T_{\text{stat}}$ we have $r_{\text{red}} \gg 1$, i.e., we obtain a significant data reduction. The overall bandwidth reduction depends on T_{stat} since D^t is ultimately determined by the time-bandwidth product $[2f_{\text{pmax}} T_{\text{stat}}]$ and the required accuracy (see (36)). For a typical scenario with the parameters shown in Table I and Table II, we obtain $D^t = 6$. With $N_{\text{bit1}} = 16$ and $N_{\text{bit2}} = 32$ $r_{\text{red}} \approx 427$, i.e., we obtain a bandwidth reduction by a factor of 427 for the PC-SDR link.

B. Complexity Reduction Analysis

Calculating the SoCE in (7) requires $\mathcal{O}(PMN)$ operations per stationarity region. The utilization of the BEM with the approximate subspace projection enables an efficient implementation of the channel emulator with reduced computational complexity. The calculation of the basis coefficients on the host computer requires only a table look-up and a scaling of P propagation graphs, i.e., it can be calculated in $\mathcal{O}(P)$ operations. The computational complexity on the FPGA is constant and *independent* from the number of propagation paths and requires $\mathcal{O}(D^t LM)$ operations. Since $D^t \ll M$ and $L \ll N$ the computational complexity of the approximate BEM is significantly smaller than the SoCE. With the parameters of Table I with $L = 40$ and $P = 500$ the complexity reduction amounts to

$$C_{\text{red}} = \frac{PNM}{P + D^t LM} \approx 267. \quad (52)$$

V. MEASUREMENT AND VALIDATION SETUP

In this Section we describe the measurement procedure and the metrics that we use for the validation of our geometry-based channel emulator. The measurement setup is shown in Fig. 7. The RUSK Lund channel sounder provides the *emulated* CIR measurements. The TX and RX of the channel sounder are connected via appropriate attenuators to the channel emulator.

We analyze the accuracy of our channel emulator by comparing the *time-variant* statistics of the emulated CIR with the simulated CIR [28], [43]. For this we use the time-variant power delay profile (PDP) and the time-variant Doppler spectral

density (DSD), which are obtained as marginals of the local scattering function (LSF) [3], [54]–[58] (see Section V-C). Please note that there is no synchronization between the measurement start of the channel sounder and the emulation start. The synchronization is performed manually in post processing.

A. Numerical Simulation

We implement a floating point simulation of (7) in MATLAB. On the host computer the channel model is updated periodically for each stationarity region s to provide $\eta_{p,s}$, $\theta_{p,s}$ and $\nu_{p,s}$. We obtain the simulated CIR using (10). For a fair comparison we limit the simulated CIR to the first L taps.

B. Emulation Parameters

For emulation, we use the channel parameters shown in Table I and the emulation parameters shown in Table II. The update rate of the coefficients is $1/T_{\text{stat}} \approx 3.907$ kHz. We set $L_{\text{pre}} = L_{\text{post}} = 4$. We use a Hann window as windowing function f_{win} (cf. (10)). We implement the model for an error of $E_{\text{th}} \leq -60$ dB. Using (36) and (37) we obtain $D^{\text{t}} = 6$ and $D^{\text{f}} = 47$. For an approximate subspace projection error smaller than E_{th} we set the resolution factor in time-direction $r^{\text{t}} = 4$ and in the frequency direction to $r^{\text{f}} = 4096$. The overall system delay $\tau_{\text{sys}} \approx 5.22 \mu\text{s}$ was measured and includes the delay introduced by the ADC and DAC, fractional decimation and first-input first-output (FIFO) register. As SDR we use an NI USRP-2954R [59] that is equipped with a Xilinx Kintex-7 FPGA.

C. Measurement Description

The RUSK channel sounder periodically samples the time-variant frequency response $g(t, f)$ of a channel to obtain the discrete time-variant frequency response $g[\chi, \omega] = g(\chi t_s, \omega f_s)$. The discrete time index $\chi \in \{0, \dots, X-1\}$ is sampled with t_s , with X being the total number of snapshots. The discrete frequency index is denoted by $\omega \in \{0, \dots, \Omega-1\}$ with Ω the number of frequency bins. The frequency resolution is defined by $f_s = B_M / \Omega$.

For the measurement, the length of the sounding sequence is set to $T = 12.8 \mu\text{s}$, which corresponds to the maximum measurable excess delay. The snapshot repetition rate is set to $t_s = 102.4 \mu\text{s}$ which results in a maximum resolvable Doppler shift $\nu_{\text{smax}} = 1/(2t_s) = 4.883$ kHz. We record $X = 10^5$ snapshots for the measurement, which is equal to a measurement time of $T_{\text{meas}} = 10.24$ s. To be able to manually synchronize the channel sounder measurement with the geometry-based channel emulator, we emulate 8 s. We set the measurement bandwidth of the channel sounder to $B_M = 100$ MHz. The bandwidth is separated in $\Omega = 1281$ frequency bins which results in $f_s = B_M / \Omega = 78.06$ kHz.

To analyze the accuracy of the geometry-based channel emulator we compare the statistics of the CIRs using the LSF [3], [54]–[58]. The LSF assumes that the fading process is locally stationary within a region of M' samples in time and N' samples in frequency. We estimate the LSF for consecutive stationarity regions in time indexed by s' . We use a multi-taper based estimator in order to obtain multiple independent spectral estimates from the same measurement [56], [60]. Since we emulate a small bandwidth, we assume only one stationarity region in frequency.

The estimate of the LSF is defined by [3], [4], [43], [58], [61]

$$\hat{\mathcal{C}}[s'; n, p] = \frac{1}{JK} \sum_{w=0}^{JK-1} \left| \mathcal{H}^{(G_w)}[s'; n, p] \right|^2. \quad (53)$$

We denote by $n \in \{0, \dots, N'-1\}$ the delay index and by $p \in \{-M'/2, \dots, M'/2-1\}$ the Doppler index, respectively. The index of each stationarity region in time is denoted by $s' \in \{0, \dots, \lfloor X/M' - 1 \rfloor\}$ and corresponds to the center of the stationarity regions. The windowed frequency response $\mathcal{H}^{(G_w)}$ is calculated from

$$\begin{aligned} \mathcal{H}^{(G_w)}[s'; n, p] = & \sum_{m''=-M'/2}^{M'/2-1} \sum_{q'=-N'/2}^{N'/2-1} g[m'' - s', q'] \\ & \cdot G_w[m'', q'] e^{-j2\pi(pm'' - nq')}, \end{aligned} \quad (54)$$

where the tapers $G_w[m'', q'] = u_i[m'', W^t, I^t]u_j[q'; W^f, I^f]$ are two-dimensional DPS sequences [3], [50]. Here $w = (i-1)I + j$, $i \in \{1, \dots, I\}$, $j \in \{1, \dots, J\}$, and $W^t = [-I/M', I/M']$, $I^t = M'$ and $W^f = [-J/N', J/N']$ and $I^f = N'$. The number of tapers in time and frequency domain is set to $I = 3$ and $J = 3$, respectively [3], [58].

The delay and Doppler shift resolutions are given by $\tau_s = 1/(N' f_s)$ and $\nu_s = 1/(M' t_s)$. Please note that for an accurate implementation of the geometry-based channel emulator the stationarity region length has to be chosen to be small enough to meet the required error threshold (cf. Section III). For the computation of the LSF, however, we chose the stationary region to be larger, to obtain a higher Doppler resolution. We set $M' = 400$, which corresponds to a stationarity region length of $T'_{\text{stat}} \approx 41$ ms in the time domain or equivalently $\nu_s \approx 24.4$ Hz. Furthermore, we set $N' = 128$, corresponding to an evaluation bandwidth of $B_{\text{eval}} \approx 10$ MHz in frequency domain or equivalently $\tau_s \approx 100$ ns.

The PDP and DSD are calculated as marginals of the LSF over the Doppler or delay domain, respectively [3], [4], [61], i.e.,

$$\hat{\mathcal{P}}_\tau[s'; n] = E_p \left\{ \hat{\mathcal{C}}[s'; n, p] \right\} = \frac{1}{M'} \sum_{p=-M'/2}^{M'/2-1} \hat{\mathcal{C}}[s'; n, p], \quad (55)$$

$$\hat{\mathcal{P}}_\nu[s'; p] = E_n \left\{ \hat{\mathcal{C}}[s'; n, p] \right\} = \frac{1}{N'} \sum_{n=0}^{N'-1} \hat{\mathcal{C}}[s'; n, p]. \quad (56)$$

We calculate the simulated CIR with the snapshot rate of the channel sounder as described above. We obtain the CTF of the simulated CIR by means of a Fourier transform. We use (53) to calculate the LSF and (55) and (56) to calculate the PDP and DSD, respectively. We define the mean error between the normalized PDPs of simulation and emulation by

$$e_\tau[s'] = \frac{1}{N'} \sum_{n=0}^{N'-1} \left\| \hat{\mathcal{P}}_\tau^{\text{SIM}, N}[s'; n] - \hat{\mathcal{P}}_\tau^{\text{EM}, N}[s'; n] \right\|, \quad (57)$$

and the error between the normalized DSDs by

$$e_\nu[s'] = \frac{1}{M'} \sum_{p=-M'/2}^{M'/2-1} \left\| \hat{\mathcal{P}}_\nu^{\text{SIM}, N}[s'; p] - \hat{\mathcal{P}}_\nu^{\text{EM}, N}[s'; p] \right\|. \quad (58)$$

The normalized PDP $\hat{\mathcal{P}}_\tau^{\text{SIM}, N}[s'; n]$ is obtained by $\hat{\mathcal{P}}_\tau^{\text{SIM}, N}[s'; n] = \hat{\mathcal{P}}_\tau^{\text{SIM}}[s'; n] / \max_{s', n}(\hat{\mathcal{P}}_\tau^{\text{SIM}}[s'; n])$. We apply the same normalization to the other PDP and to the DSDs. For the calculation

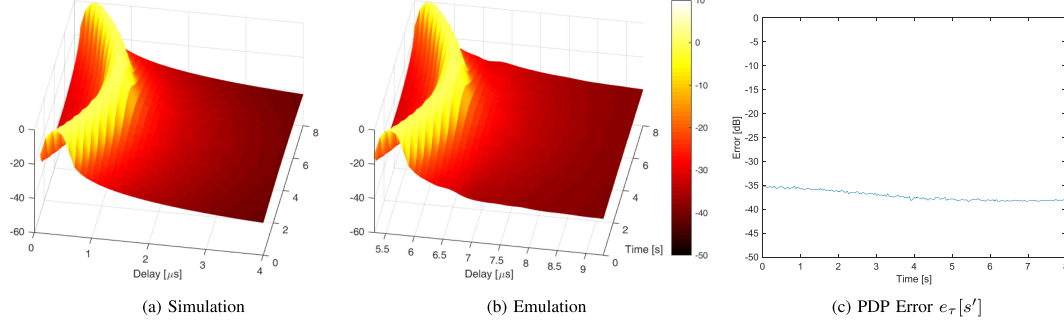


Fig. 8. Comparison of the normalized PDPs for one propagation path with changing Doppler shift from -2 kHz to 2 kHz .

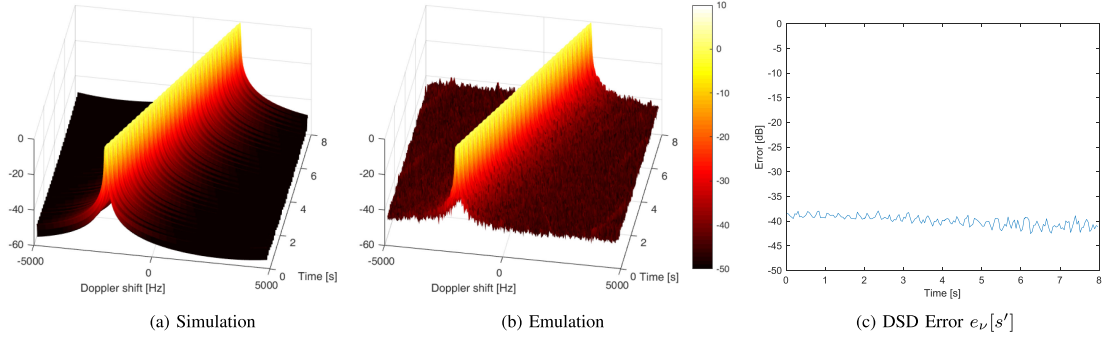


Fig. 9. Comparison of the normalized DSDs for one propagation path with changing Doppler shift from -2 kHz to 2 kHz .

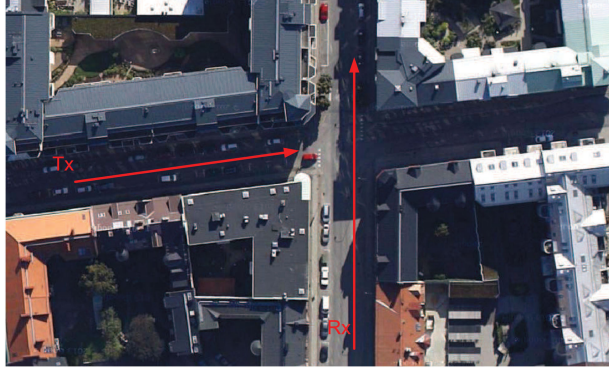


Fig. 10. Top view of the investigated intersection ($N55^{\circ} 42' 38''$, $E13^{\circ} 11' 14''$) in the city of Lund with the trajectories of TX and RX respectively [36].

of the error we manually synchronize the simulation and the emulation.

VI. MEASUREMENT RESULTS

We validate our channel emulator with two different scenarios: (a) the emulation of a single path with continuously changing path delay, and (b) a GSCM of a road intersection. We compare the emulated CIR with the simulated CIR by means of the time-variant PDP and DSD, see (57) and (58). In the Appendix the backward compatibility of the geometry-based channel emulator is shown by the emulation of ETSI channel models.

A. One-Path Channel Model

First, we validate the fundamental capability of our geometry-based channel emulator to emulate continuously changing path

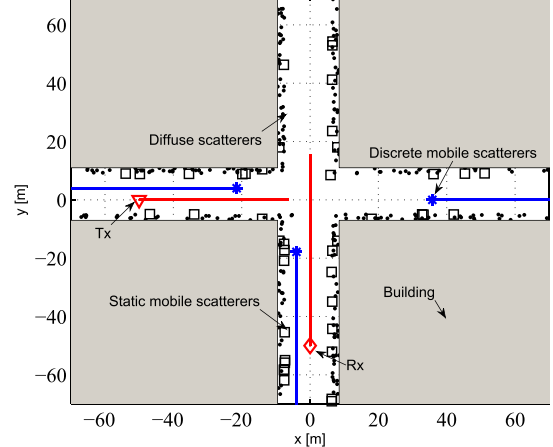


Fig. 11. Scatterer distribution of the channel model for a road intersection [36].

delays. We emulate a single propagation path with a Doppler shift that changes from -2 kHz to 2 kHz . This leads to a continuously changing path delay that increases and decreases, according to the current Doppler shift. In Fig. 8, we show from left to right (a) the normalized PDP from the simulated CIR, (b) the normalized PDP from the emulated CIR, and (c) the error between the normalized PDPs. We show the same plots for the DSDs in Fig. 9.

The results show a mean error of $\approx -40\text{ dB}$ between the DSDs and $\approx -35\text{ dB}$ between the PDPs. We obtain an error above the intended error threshold of -60 dB due to additive measurement noise during the measurement shown, e.g., in the DSD of the emulator measurement in Fig. 9(b). With $M' = 400$

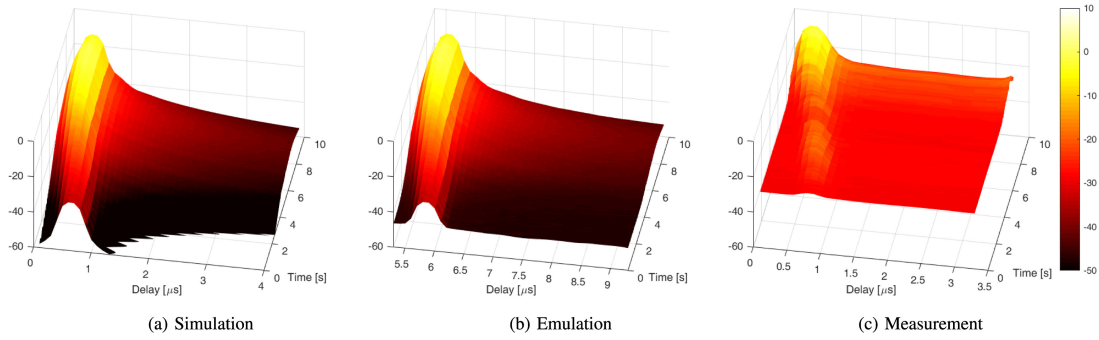


Fig. 12. Comparison of the normalized PDPs of the simulation and emulation of the GSCM for the road intersection scenario and the corresponding measurement in Lund.

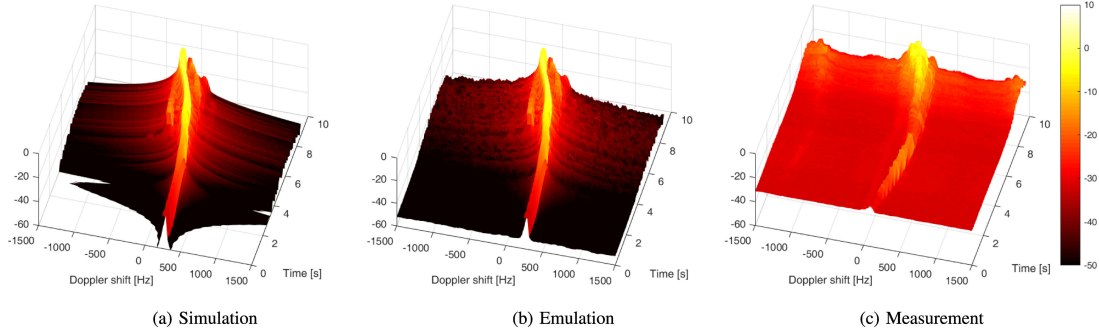


Fig. 13. Comparison of the normalized DSDs of the simulation and emulation of the GSCM for the road intersection scenario and the corresponding measurement in Lund.

and $N' = 128$ we obtain a $10 \log_{10}(400/128) \approx 5$ dB smaller mean error of the DSDs compared to the mean error of the PDPs, which is reflected in the measurement results. The small change of the mean error over time is due to imperfect synchronization in post processing.

B. Geometry-Based Stochastic Channel Model

We show the capability of our geometry-based channel emulator to emulate realistic propagation scenarios, by the emulation of a GSCM of a road intersection scenario in *real-time*. The selected intersection with the trajectories of the TX and the RX is shown in Fig. 10. Empirical channel measurement data of the intersection was obtained by channel measurements performed in the city of Lund, Sweden in 2009 [3], [5].

In [36] a GSCM for this intersection crossing scenario has been developed. The model comprises up to 617 active propagation paths, each path having a time-variant Doppler shift, delay and attenuation. We determine the number of active paths by a visibility check between TX and RX. The GSCM includes randomly placed scatterers that are subject to a statistical distribution [35]. The geometry and one random realization of the point scatterer distribution are shown in Fig. 11. In [36] the delay-spread and path-loss versus distance is compared with the measurement data and a good match is demonstrated. We added a diffraction model for the corners of the buildings to further improve the non-line of sight (NLOS) to line of sight (LOS) transition [62].³

³It is based on the assumption that diffraction can take place at a street corner when LOS is unavailable. The attenuation of the diffraction path is calculated by the free space path loss expression and a fictitious distance, which is given by Berg's recursive expression [63]. The detailed calculation of the fictitious distance can be found in [62].

In Fig. 12, we show from left to right the normalized PDP of (a) the simulated GSCM, (b) the emulated GSCM, and (c) the road intersection measurement. In Fig. 13, we show the same comparison for the DSD. The mean error between the normalized PDPs and DSDs of emulation and simulation are shown in Fig. 14. The mean error shows a good match between the numerical simulation and emulation. The error above the intended threshold of -60 dB is due to measurement noise (see Section VI-A).

We analyze the non-stationary fading process of the GSCM using statistical quantities, i.e., the time-variant root mean square (RMS) delay spread and the time-variant RMS Doppler spread. The RMS spreads are calculated according to [3]. We apply a noise-power threshold to the emulated results to eliminate noise components that could be mistaken as multi-path components. The noise-power threshold is chosen 5 dB above the noise floor. The sensitivity-threshold is chosen 30 dB from the highest peak (cf. [3], [64]). For the evaluation of the intersection measurements the high Doppler components are excluded.⁴

In Fig. 15, the gray region represents the 99 % quantiles of (a) the time-variant RMS delay spread and (b) the time-variant RMS Doppler spread, obtained from 100 random realizations of the GSCM scatterer placement. We plot the same second order statistics for the simulation of the GSCM (Simulation), the emulation of the GSCM (Emulation) and the road intersection

⁴In our channel measurement data of the road intersection shown in Fig. 13(c), there are Doppler components visible at ± 1500 Hz starting from second nine onwards. We attribute the components to interference and did not include them in our GSCM model. The reason for this is, that the car during the measurement was traveling at max. 60 km/h (16.7 m/s). The visible Doppler components would be caused by a velocity of 79 m/s, which is not realistic, even if multiple reflections were considered. Hence, we are sure that these components are caused by interference.

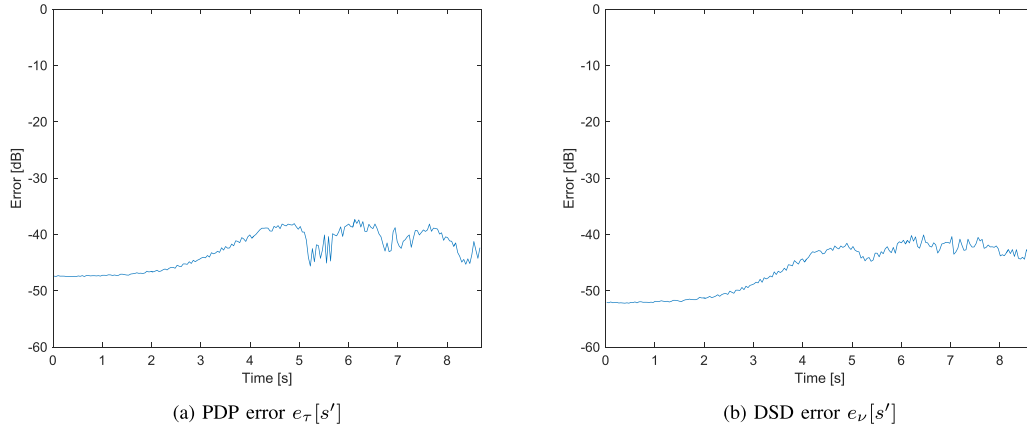


Fig. 14. PDP and DSD error between simulation and emulation for a road intersection scenario.

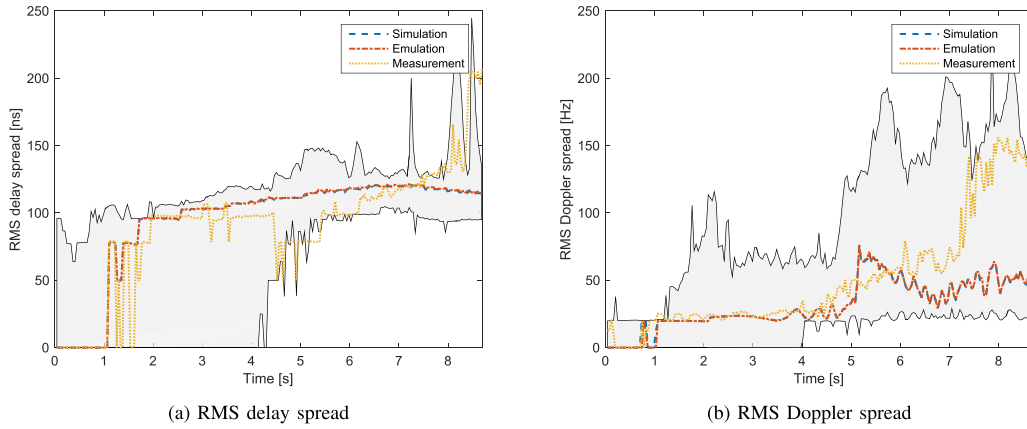


Fig. 15. Comparison of the second order statistics of the road intersection scenario.

measurement (Measurement). From Fig. 15 we observe that the RMS delay and Doppler spread curves of numerical simulation and emulation match closely, they lay on top of each other. For the GSCM a random realization of the scatterer placement is utilized. The road intersection measurement corresponds to another scatter placement. Hence, the RMS delay and Doppler spread of simulation and emulation differ from the RMS delay and Doppler spread of the measurement. However, the measured RMS delay and Doppler spread are well within the gray region, showing that our GSCM parameterization can model the road intersection scenario. Further statistical evaluations of the measured RMS delay and RMS Doppler spreads in other scenarios can be found in [3].

Our geometry-based channel emulator measurement results demonstrate the capability to emulate a large number of propagation paths with continuously changing path delays and Doppler shifts that are determined by the environment geometry. Hence, we showed that the geometry-based channel emulator is able to emulate non-stationary wireless communication channels.

VII. CONCLUSION

In this paper we presented a real-time geometry-based channel emulator, that enables the emulation of non-stationary doubly-selective fading channels on an SDR. Our emulator directly uses a propagation path based geometric model that allows for continuously changing path delays and Doppler shifts. The

emulator is split into two components, a propagation module, calculated on a general purpose multicore PC and a convolution module, implemented on the SDR. The emulator uses a reduced-rank BEM to compress and transmit the CIR from the PC to the SDR, where it is decompressed and convolved with the input signal to produce the intended output signal. Our algorithm obtains a data rate reduction of more than two orders of magnitude for the communication link from the PC to the SDR unit. For the reduced-rank BEM we provide the mathematical theory as well as a detailed error analysis. We measured the emulated CIR with the RUSK Lund channel sounder for a vehicular scenario with 617 propagation paths. A comparison of the time-variant PDP and DSD of simulated and emulated CIR showed a close match with an error smaller than -35 dB. Our channel emulator is able to accurately emulate non-stationary fading channels with continuously changing path delays and Doppler shifts in real-time.

APPENDIX ETSI TDL CHANNEL MODELS

To demonstrate the backward compatibility of the geometry-based channel emulator to emulate TDL models, we emulate the ETSI channel models for testing vehicular communication systems [19], [24]. The models are TDL based and consider channel statistics that do not change over time. The DSD of the delay taps is modeled as a half-bathtub spectrum or as a

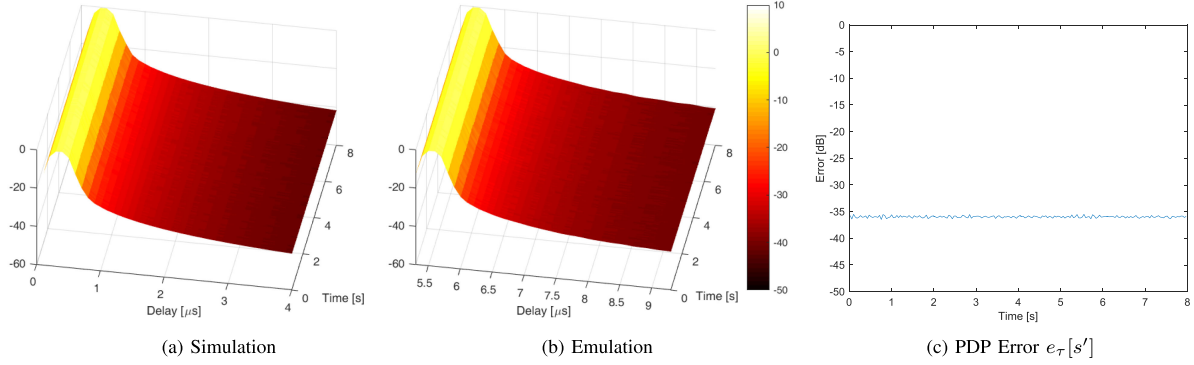


Fig. 16. Comparison of the normalized PDPs of ETSI channel model rural LOS.

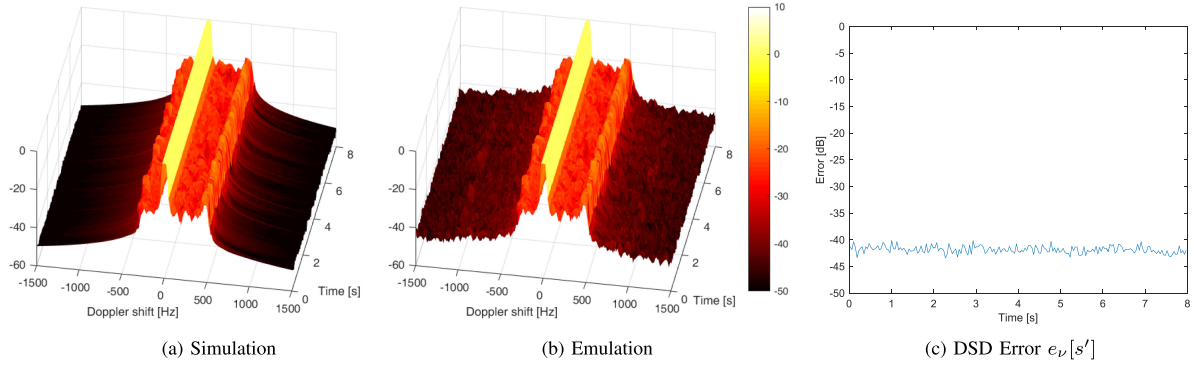


Fig. 17. Comparison of the normalized DSDs of ETSI channel model rural LOS.

full-bathtub spectrum depending on the scenario considered. There exist five scenarios, each defining different path delays and Doppler spectra for the corresponding paths. We emulated and measured all scenarios. Due to space constraints we only show the rural LOS scenario. We implement the positive (negative) half bathtub spectrum by summing 40 propagation paths for each delay tap and adjusting the impinging angle of the paths to the right (left) hemisphere corresponding to positive (negative) Doppler shifts. The impinging angles are randomly distributed on the respective hemisphere. The normalized PDPs and DSDs, and the error are shown in Fig. 16 and Fig. 17, respectively. Also here we see a close match between simulation and emulation.

ACKNOWLEDGMENT

The authors would like to thank O. Renaudin for valuable discussions and C. Gustafson and J. Flordelis for their collaboration during the measurements.

REFERENCES

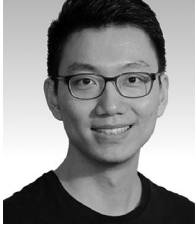
- [1] ITU, “Minimum requirements related to technical performance for IMT-2020 radio interface(s),” Int. Telecommun. Union, Geneva, Switzerland, Tech. Rep. M.2410-0 (11/2017), 2017.
- [2] M. Shaf *et al.*, “5G: A tutorial overview of standards, trials, challenges, deployment, and practice,” *IEEE J. Sel. Areas Commun.*, vol. 35, no. 6, pp. 1201–1221, Jun. 2017.
- [3] L. Bernadó, T. Zemen, F. Tufvesson, A. F. Molisch, and C. F. Mecklenbräuker, “Delay and Doppler spreads of nonstationary vehicular channels for safety-relevant scenarios,” *IEEE Trans. Veh. Technol.*, vol. 63, no. 1, pp. 82–93, Jan. 2014.
- [4] L. Bernadó, T. Zemen, F. Tufvesson, A. F. Molisch, and C. F. Mecklenbräuker, “Time- and frequency-varying K -factor of non-stationary vehicular channels for safety-relevant scenarios,” *IEEE Trans. Intell. Transp. Syst.*, vol. 16, no. 2, pp. 1007–1017, Apr. 2015.
- [5] A. Paier, L. Bernadó, J. Karedal, O. Klemp, and A. Kwoczek, “Overview of vehicle-to-vehicle radio channel measurements for collision avoidance applications,” in *Proc. IEEE 71st Veh. Technol. Conf.*, Taipei, Taiwan, May 2010, pp. 1–5.
- [6] O. Renaudin, V.-M. Kolmonen, P. Vainikainen, and C. Oestges, “Wideband MIMO car-to-car radio channel measurements at 5.3 GHz,” in *Proc. IEEE 68th Veh. Technol. Conf.*, 2008, pp. 1–5.
- [7] J. Karedal *et al.*, “Radio channel measurements at street intersections for vehicle-to-vehicle safety applications,” in *Proc. IEEE 71st Veh. Technol. Conf.*, May 2010, pp. 1–5.
- [8] C. F. Mecklenbrauker *et al.*, “Vehicular channel characterization and its implications for wireless system design and performance,” *Proc. IEEE*, vol. 99, no. 7, pp. 1189–1212, Jul. 2011.
- [9] W. Viriyasitavat, M. Boban, H. M. Tsai, and A. Vasilakos, “Vehicular communications: Survey and challenges of channel and propagation models,” *IEEE Veh. Technol. Mag.*, vol. 10, no. 2, pp. 55–66, Jun. 2015.
- [10] P. Unterhuber *et al.*, “A survey of channel measurements and models for current and future railway communication systems,” *Mob. Inf. Syst.*, vol. 2016, 2016, Art. no. 7308604.
- [11] Accessed: Jan. 15, 2017. [Online]. Available: <http://www.spirent.com/>
- [12] Accessed: Jan. 15, 2017. [Online]. Available: <http://www.anite.com/>
- [13] Real-Time MIMO Channel Emulation on the NI PXIe-5644R, Nat. Instrum. May 2013. [Online]. Available: <http://www.ni.com/example/31556/en/>. Accessed: Jan. 15, 2016.
- [14] D. Vlastaras, S. Malkowsky, and F. Tufvesson, “Stress test of vehicular communication transceivers using software defined radio,” in *Proc. IEEE 81st Veh. Technol. Conf.*, vol. 41, no. 2, May 2015, pp. 1–4.
- [15] G. Ghiaasi, M. Ashury, D. Valstaras, M. Hofer, Z. Xu, and T. Zemen, “Real-time vehicular channel emulator for future conformance tests of wireless ITS modems,” in *Proc. 10th Eur. Conf. Antennas Propag.*, Apr. 2016, pp. 1–5.
- [16] “MKG Sys,” [Online]. Available: <https://www.mkgsys.com/>. Accessed: Jan. 15, 2016.

- [17] T. Fernández-Caramés, M. González-López, and L. Castedo, "FPGA-based vehicular channel emulator for real-time performance evaluation of IEEE 802.11p transceivers," *EURASIP J. Wireless Commun. Netw.*, vol. 2010, no. 1, 2010, Art. no. 607467.
- [18] J. Matai, P. Meng, L. Wu, B. Weals, and R. Kastner, "Designing a hardware in the loop wireless digital channel emulator for software defined radio," in *Proc. Int. Conf. Field-Prog. Technol.*, Dec. 2012, pp. 206–214.
- [19] T. Blazek, C. Mecklenbräuker, G. Ghiaasi, D. Smely, and M. M. Ashury, "Vehicular channel models: A system level performance analysis of tapped delay line models," in *Proc. IEEE Proc. 15th Int Conf. ITS Telecommun.*, Warsaw, Poland, 2017, pp. 1–8.
- [20] G. Ghiaasi, T. Blazek, M. Ashury, S. R. Ramalho, and C. Mecklenbräuker, "Real-time emulation of nonstationary channels in safety-relevant vehicular scenarios," *Wireless Commun. Mobile Comput.*, vol. 2018, Feb. 2018, Art. no. 2423837.
- [21] Q. Zhu *et al.*, "A novel 3D non-stationary wireless MIMO channel simulator and hardware emulator," *IEEE Trans. Commun.*, vol. 66, no. 9, pp. 3865–3878, Sep. 2018.
- [22] Z. Xu, M. Gan, and T. Zemen, "Cluster-based non-stationary vehicular channel model," in *Proc. 10th Eur. Conf. Antennas Propag.*, Apr. 2016, pp. 1–5.
- [23] Z. Xu, M. Gan, C. F. Mecklenbraeuker, and T. Zemen, "Cluster spreads for time-variant vehicular channels," in *Proc. 9th Eur. Conf. Antennas Propag.*, May 2015, pp. 1–5.
- [24] "ETSI TS 103 257 - Intelligent Transport Systems (ITS); Access Layer; ITS-G5 Channel Models and Performance Analysis Framework," Mar. 2017.
- [25] F. Kaltenberger, T. Zemen, and C. W. Ueberhuber, "Low-complexity geometry-based MIMO channel simulation," *EURASIP J. Adv. Signal Process.*, vol. 2007, no. 1, 2007, Art. no. 095281.
- [26] F. Kaltenberger, "Low complexity simulation of wireless channels using discrete prolate spheroidal sequences," Ph.D. dissertation, Tech. Univ. Vienna, Wien, Austria, May 2007.
- [27] F. Kaltenberger, G. Steinböck, G. Humer, and T. Zemen, "Low-complexity geometry based MIMO channel emulation," *Proc. 1st Eur. Conf. Antennas Propag.*, vol. 626, Oct. 2006, pp. 1–8.
- [28] M. Hofer, Z. Xu, and T. Zemen, "Real-time channel emulation of a geometry-based stochastic channel model on a SDR platform," in *Proc. IEEE 18th Int. Workshop Signal Process. Adv. Wireless Commun.*, Sapporo, Japan, Jul. 2017, pp. 1–5.
- [29] J. Maurer, "Strahlenoptisches Kanalmodell fuer die Fahrzeug-Fahrzeug-Funkkommunikation," Ph.D. dissertation, Univ. Karlsruhe, Karlsruhe, Germany, 2005.
- [30] J. Maurer, T. Fugen, and W. Wiesbeck, "Narrow-band measurement and analysis of the inter-vehicle transmission channel at 5.2 GHz," in *Proc. IEEE 55th Veh. Technol. Conf.*, vol. 3, 2002, pp. 1274–1278.
- [31] J. Maurer, T. M. Schafer, and W. Wiesbeck, "A realistic description of the environment for inter-vehicle wave propagation modelling," in *Proc. IEEE 54th Veh. Technol. Conf.*, vol. 3, 2001, pp. 1437–1441.
- [32] J. Maurer, T. Fugen, T. Schafer, and W. Wiesbeck, "A new inter-vehicle communications (IVC) channel model," in *Proc. IEEE 60th Veh. Technol. Conf.*, vol. 1, Sep. 2004, pp. 9–13.
- [33] Z. Yun and M. F. Iskander, "Ray tracing for radio propagation modeling: Principles and applications," *IEEE Access*, vol. 3, pp. 1089–1100, 2015.
- [34] M. Gan, "Accurate and low-complexity ray tracing channel modeling," Ph.D. dissertation, Technical Univ. Vienna, Vienna, Austria, 2015.
- [35] J. Karedal *et al.*, "A geometry-based stochastic MIMO model for vehicle-to-vehicle communications," *IEEE Trans. Wireless Commun.*, vol. 8, no. 7, pp. 3646–3657, Jul. 2009.
- [36] Z. Xu *et al.*, "Relaying for IEEE 802.11p at road intersection using a vehicular non-stationary channel model," in *Proc. 6th Int. Symp. Wireless Veh. Commun.*, Vancouver, Canada, Sep. 2014, pp. 1–6.
- [37] K. Mahler, W. Keusgen, F. Tufvesson, T. Zemen, and G. Caire, "Measurement-based wideband analysis of dynamic multipath propagation in vehicular communication scenarios," *IEEE Trans. Veh. Technol.*, vol. 66, no. 6, pp. 4657–4667, Jun. 2017.
- [38] R. He *et al.*, "A dynamic wideband directional channel model for vehicle-to-vehicle communications," *IEEE Trans. Ind. Electron.*, vol. 62, no. 12, pp. 7870–7882, Dec. 2015.
- [39] P. Almers *et al.*, "Survey of channel and radio propagation models for wireless MIMO systems," *EURASIP J. Wireless Commun. Netw.*, vol. 2007, no. 1, Feb. 2007, Art. no. 019070.
- [40] X. Liang, X. Zhao, S. Li, Q. Wang, and W. Lu, "A 3D geometry-based scattering model for vehicle-to-vehicle wideband MIMO relay-based cooperative channels," *China Commun.*, vol. 13, no. 10, pp. 1–10, Oct. 2016.
- [41] M. Zhu, G. Eriksson, and F. Tufvesson, "The COST 2100 channel model: Parameterization and validation based on outdoor MIMO measurements at 300 MHz," *IEEE Trans. Wireless Commun.*, vol. 12, no. 2, pp. 888–897, Feb. 2013.
- [42] W. I. WP5, "Final report on link level and system level channel models," Nov. 2005.
- [43] M. Hofer *et al.*, "Validation of a real-time geometry-based stochastic channel model for vehicular scenarios," in *Proc. IEEE 87th Veh. Technol. Conf.*, Jun. 2018, pp. 1–5.
- [44] T. Zemen, L. Bernadó, N. Czink, and A. Molisch, "Iterative time-variant channel estimation for 802.11p using generalized discrete prolate spheroidal sequences," *IEEE Trans. Veh. Technol.*, vol. 61, no. 3, pp. 1222–1233, Mar. 2012.
- [45] N. Czink, F. Kaltenberger, Y. Zhou, L. Bernadó, T. Zemen, and X. Yin, "Low-complexity geometry-based modeling of diffuse scattering," *Proc. 4th Eur. Conf. Antennas Propag.*, 2010, pp. 1–4.
- [46] D. Tse and P. Viswanath, *Fundamentals of Wireless Communication*. New York, NY, USA: Cambridge Univ. Press, 2005.
- [47] F. Hlawatsch and G. Matz, *Wireless Communications Over Rapidly Time-Varying Channels*, 1st ed. New York, NY, USA: Academic, 2011.
- [48] M. Walter, T. Zemen, and D. Shutin, "Empirical relationship between local scattering function and joint probability density function," in *Proc. IEEE 26th Int. Symp. Pers. Indoor Mobile Radio Commun.*, Aug. 2015, pp. 542–546.
- [49] M. Walter, D. Shutin, and A. Dammann, "Time-variant Doppler PDFs and characteristic functions for the vehicle-to-vehicle channel," *IEEE Trans. Veh. Technol.*, vol. 66, no. 12, pp. 10748–10763, Dec. 2017.
- [50] D. Slepian, "Prolate spheroidal wave functions, Fourier analysis, and uncertainty-V: The discrete case," *Bell Syst. Techn. J.*, vol. 57, no. 5, pp. 1371–1430, May 1978.
- [51] F. Kaltenberger, T. Zemen, and C. Ueberhuber, "Low-complexity doubly selective channel simulation using multidimensional discrete prolate spheroidal sequences," in *Proc. 15th IST Mobile Wireless Commun. Summit*, 2006, pp. 1–5.
- [52] T. Zemen, C. Mecklenbraeuker, F. Kaltenberger, and B. Fleury, "Minimum-energy band-limited predictor with dynamic subspace selection for time-variant flat-fading channels," *IEEE Trans. Signal Process.*, vol. 55, no. 9, pp. 4534–4548, Sep. 2007.
- [53] T. Zemen and A. Molisch, "Adaptive reduced-rank estimation of nonstationary time-variant channels using subspace selection," *IEEE Trans. Veh. Technol.*, vol. 61, no. 9, pp. 4042–4056, Nov. 2012.
- [54] G. Matz, "On non-WSSUS wireless fading channels," *IEEE Trans. Wireless Commun.*, vol. 4, no. 5, pp. 2465–2478, Sep. 2005.
- [55] G. Matz, "Doubly underspread non-WSSUS channels: Analysis and estimation of channel statistics," in *Proc. IEEE 4th Int. Workshop Signal Process. Adv. Wireless Commun.*, Jun. 2003, pp. 190–194.
- [56] D. J. Thomson, "Spectrum estimation and harmonic analysis," *Proc. IEEE*, vol. 70, no. 9, pp. 1055–1096, Sep. 1982.
- [57] L. Bernado, T. Zemen, A. Paier, J. Karedal, and B. H. Fleury, "Parametrization of the local scattering function estimator for vehicular-to-vehicular channels," in *Proc. IEEE 70th Veh. Technol. Conf.*, Sep. 2009, pp. 1–5.
- [58] L. Bernadó, T. Zemen, F. Tufvesson, A. F. Molisch, and C. F. Mecklenbraeuker, "The (in-) validity of the WSSUS assumption in vehicular radio channels," in *Proc. IEEE 23rd Int. Symp. Pers. Indoor Mob. Radio Commun.*, Sep. 2012, pp. 1757–1762.
- [59] Device Specifications, "NI USRP-2594R, 10 MHz to 6 GHz Tunable RF Transceiver," Nat. Instrum., Austin, TX, USA.
- [60] D. B. Percival and A. T. Walden, *Spectral Analysis for Physical Applications: Multitaper and Conventional Univariate Techniques*. Cambridge, U.K.: Cambridge Univ. Press, 1993.
- [61] E. Zoechmann *et al.*, "Measured delay and Doppler profiles of overtaking vehicles at 60 GHz," in *Proc. 12th Eur. Conf. Antennas Propag.*, Apr. 2018, pp. 1–5.
- [62] METIS, Deliverable D1.4 - METIS channel models. Jul. 2015. [Online]. Available: https://www.metis2020.com/wp-content/uploads/METIS_D1_4_v3.pdf
- [63] J. E. Berg, "A recursive method for street microcell path loss calculations," in *Proc. IEEE 1995 6th Int. Symp. Pers. Indoor Mobile Radio Commun.*, vol. 1, Sep. 1995, pp. 140–143.
- [64] L. Bernado *et al.*, "In-tunnel vehicular radio channel characterization," in *Proc. IEEE 73rd Veh. Technol. Conf.*, May 2011, pp. 1–5.



Markus Hofer received the Dipl.-Ing. degree (with distinction) in telecommunications from the Vienna University of Technology, Wien, Austria, in 2013. Since 2013, he has been working toward the Ph.D. degree in telecommunications. From 2013 to 2015, he was with the Telecommunications Research Center, Vienna working as a Researcher in “Signal and Information Processing” Department. Since 2015, he has been with the AIT Austrian Institute of Technology as a Junior Scientist in the Research Group for ultrareliable wireless machine-to-machine communications.

His research interests include low-latency wireless communications, vehicular channel measurements, modeling and emulation, time-variant channel estimation, mmWave, massive MIMO, cooperative communication systems, and interference management.

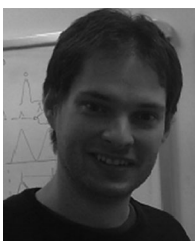


Zhinan Xu received the M.Sc. degree in wireless communications from Lund university, Lund, Sweden, in 2011 and the Ph.D. degree in telecommunications from the Vienna University of Technology, Vienna, Austria, in 2016. From 2008 to 2009, he worked as Mobile Network Engineer with Huawei Technologies, Shenzhen, China. From 2011 to 2015, he was with the Telecommunications Research Center Vienna working as a Researcher in “Signal and Information Processing” Department. From 2015 to 2016, he was with AIT Austrian Institute of Technology as a Scientist in the research group for ultrareliable wireless machine-to-machine communications.

His research interests include interference management, cooperative communication systems, vehicular communications, and channel modeling.



Dimitrios Vlastaras received the master’s degree in computer science and engineering and a Licentiate degree in electrical engineering, both from Lund University, Lund, Sweden, in 2014 and 2017, respectively. He started his career in wireless systems working as a Systems Tester for Ericsson Mobile Platforms in 2008. He is currently working with 5G as a Systems Designer at Ericsson, Lund.



Bernhard Schrenk (S’10–M’11) was born in Austria, in 1982. He received the M.Sc. degree in microelectronics from the Technical University of Vienna, Wien, Austria, in 2007. In 2011, he received the Ph.D. degree from UPC BarcelonaTech, Spain. His Ph.D thesis on multifunctional optical network units for next-generation Fiber-to-the-Home access networks was carried out within the FP7 SARDANA and EURO-FOS projects. He was with the Institute of Experimental Physics of Prof. A. Zeilinger, where he was involved in the realization of a first commercial prototype for a quantum cryptography system, within the European SECOQC Project. In 2011, he joined the Photonic Communications Research Laboratory, NTUA, Athens, as Postdoctoral Researcher and established his research activities on coherent FTTH under the umbrella of the FP7 GALACTICO Project. In 2013, he established his own research force on photonic communications at AIT Austrian Institute of Technology, Vienna, where he is working toward next-generation metro-access-5G networks, photonics integration technologies and quantum optics. He has authored and coauthored 125 publications in top-of-the-line (IEEE, OSA) journals and presentations in the most prestigious and highly competitive optical fiber technology conferences. He was further awarded with the Photonics21 Student Innovation Award and the Euro-Fos Student Research Award for his Ph.D. thesis, honoring not only his R&D work but also its relevance for the photonics industry. He was elected as Board-of-Stakeholder member of the Photonics21 European Technology Platform in 2017. During his extensive research activities he was and is still engaged in several European projects such as SARDANA, BONE, BOOM, APACHE, GALACTICO, EURO-FOS, and the Quantum Flagship Project UNIQORN. In 2013, he received the European Marie-Curie Integration Grant WARP-5. In 2018, he was awarded by the European Research Council with the ERC Starting Grant COYOTE, which envisions coherent optics everywhere.



David Löschchenbrand received the Dipl.-Ing. degree (with distinction) in telecommunications from the TU Wien, Wien, Austria, in 2016. From 2012 to 2015, he worked with the Institute of Telecommunications, TU Wien on antenna measurements and characterization. Since 2016, he has been with the AIT Austrian Institute of Technology as a Junior Scientist in the research group for ultrareliable wireless machine-to-machine communications. His research interests include massive MIMO, vehicular channel measurements and modeling, and real-time signal processing.



Fredrik Tufvesson received the Ph.D. degree from Lund University, Lund, Sweden, in 2000. After two years at a startup company, he joined the Department of Electrical and Information Technology, Lund University, where he is currently a Professor of radio systems. His main research interests include interplay between the radio channel and the rest of the communication system with various applications in 5G systems such as massive MIMO, mm wave communication, vehicular communication, and radio-based positioning.

He has authored around 80 journal papers and 140 conference papers, he recently got the Neal Shepherd Memorial Award for the best propagation paper in IEEE TRANSACTIONS ON VEHICULAR TECHNOLOGY and the IEEE Communications Society Best Tutorial Paper Award.



Thomas Zemen (S’03–M’05–SM’10) received the Dipl.-Ing. degree (with distinction) in electrical engineering in 1998, the Doctoral degree (with distinction) in 2004, and the Venia Docendi (Habilitation) for “Mobile Communications” in 2013, all from the Vienna University of Technology, Wien, Austria.

Since 2014, he has been a Senior Scientist at AIT Austrian Institute of Technology, Vienna, Austria, leading the Reliable Wireless Communications Group. He took on the role of thematic coordinator for physical layer security in 2018. From 2003

to 2014, he was with FTW Forschungszentrum Telekommunikation Wien heading the “Signal and Information Processing” Department since 2008. From 1998 to 2003, he worked as a Hardware Engineer and Project Manager for the Radio Communication Devices Department, Siemens, Austria. He has authored four book chapters, 35 journal papers, and more than 105 conference communications for which he also served as a Reviewer. He holds two patents in the field of wireless communications. His research interests focus on wireless ultrareliable low-latency communications system for autonomous vehicles and industrial production environments, massive MIMO systems, time-variant channel measurements, modeling and real time emulation, software-defined radio rapid prototyping, and indoor localization.

Dr. Zemen is an external Lecturer with the Vienna University of Technology and served as an Editor for the IEEE TRANSACTIONS ON WIRELESS COMMUNICATIONS from 2011 to 2017. He is a member of the European Association for Signal Processing and Strategic Advisor to the Austrian Federal Ministry for Transport, Innovation and Technology (BMVIT) for intelligent transportation systems.